ELSEVIER

Journal of Fluids and Structures 24 (2008) 183–199

JOURNAL OF FLUIDS AND STRUCTURES

www.elsevier.com/locate/jfs

Effect of spanwise flexibility on flapping wing propulsion

S. Heathcote, Z. Wang, I. Gursul*

Department of Mechanical Engineering, University of Bath, Bath, BA2 7AY, UK

Received 20 November 2006; accepted 10 August 2007
Available online 1 October 2007

Abstract

A water tunnel study of the effect of spanwise flexibility on the thrust, lift and propulsive efficiency of a rectangular wing oscillating in pure heave has been performed. The thrust and lift forces were measured with a force balance, and the flow field was measured with a Particle Image Velocimetry system. Introducing a degree of spanwise flexibility was found to be beneficial. For Strouhal numbers greater than 0.2, a degree of spanwise flexibility was found to yield a small increase in thrust coefficient, and a small decrease in power-input requirement, resulting in higher efficiency. In this case, a moderately stronger trailing-edge vortex system was observed. Introducing a far greater degree of spanwise flexibility, however, was found to be detrimental. A large phase delay of the wing tip displacement was observed, leading to the root and tip moving in opposite directions for a significant portion of the flapping stroke. Vorticity of opposing sign was observed to be shed from the root and tip, resulting in a weak and fragmented vorticity pattern. The thrust coefficient was observed to be significantly reduced, and the efficiency diminished. It is noted that the range of Strouhal numbers for which spanwise flexibility was found to offer benefits overlaps the range found in nature, of $0.2 < \mathrm{Sr} < 0.4$. From a design aspect, flexibility may benefit flapping-wing Micro Air Vehicles both aerodynamically and in the inherent lightness of flexible structures.

Keywords: Vortex flows; Flapping wings; Heave; Thrust; Propulsive efficiency; Wing flexibility.

1. Introduction

There is great interest in small (wing-span less than six inches) radio-controlled aircraft known as *Micro Air Vehicles* (MAVs). Many applications have been suggested for a MAV carrying a miniature video camera or other sensing device. One specific example from industry would be the surveying of a chemical refinery following a storm. Civil and military applications have also been suggested. The majority of MAV applications require great manoeuvrability, and some demand the ability to hover. The wonderful agility of birds, bats, and insects has led to the design of flapping wing MAVs (Spedding and Lissaman, 1998; Shyy et al., 1999). For this reason, research on flapping wing propulsion has attracted considerable attention recently. Because of the small length scales involved, the Reynolds number is low, typically of order 10^3–10^5.

The origin of thrust for an oscillating airfoil was found by Knoller (1909), and later and independently by Betz (1912). The *Knoller–Betz* effect was demonstrated in a wind tunnel experiment by Katzmayr (1922). Following this, a number of

*Corresponding author.
E-mail address: ensiag@bath.ac.uk (I. Gursul).

0889-9746/$ - see front matter
doi:10.1016/j.jfluidstructs.2007.08.003

Nomenclature

a	amplitude
b	wing span
c	chord length
C_T	thrust coefficient
C_P	power coefficient
F	force per unit span
h	root amplitude (a_{ROOT}/c)
k_G	Garrick reduced frequency ($\pi fc/U_0$)
Re	Reynolds number (U_0c/v)
s	displacement
Sr	Strouhal number ($2fa_{\mathrm{MID}}/U_0$)
t	time
T	thrust per unit span; period
U_0	freestream velocity
v	wing root velocity
η	propulsive efficiency
μ	viscosity
ρ	density
φ	tip phase angle
ω	heave angular frequency
Ω	vorticity

Subscripts

x	streamwise direction
y	lateral direction
z	spanwise direction

theoretical and numerical models of oscillating airfoils were developed. These early models, by Garrick (1936), Lighthill (1970), and Wu (1971), were of thin, 2-D airfoils, oscillating in inviscid flow. Consequently, they significantly overestimated the propulsive efficiency (Isogai et al., 1999; Ramamurti and Sandberg, 2001) in the low-Reynolds-number separated flows observed in natural flight, and in the flight of MAVs (Jones et al., 2001a). More recently, Navier–Stokes simulations (Tuncer and Platzer, 1996) have yielded more accurate flow pattern and propulsive efficiency predictions.

Experiments have focused on rigid airfoils (Koochesfahani, 1989; Jones et al., 1998; Lai and Platzer, 1999), where the effects of oscillation mode (e.g. pure heave, pure pitch, Emblemsvag et al., 2003; coupled heave and pitch, Anderson et al., 1998), (Hover et al., 2004) (e.g. sine wave, triangle wave), and aspect ratio (Jones et al., 2002) have been investigated. The special case of hovering flight has also received attention (Freymuth, 1990; Sunada et al., 2001). The effect of wing stiffness, in either the chordwise or spanwise direction, is relatively unexplored. This is surprising given the importance of flexibility to fish (Triantafyllou et al., 2000), and the finding of intricate variations in the stiffness of insect wings (Wootton, 1981)—though the role of flexibility in insect flight is still unclear (Maxworthy, 1981).

The effect of chordwise flexibility for an airfoil in heave at low Reynolds numbers has been studied by Heathcote and Gursul (2006). A schematic of the 2-D experiment is shown in Fig. 1(a). The airfoil comprises a tear-drop solid aluminium leading edge followed by a flexible steel plate. The airfoil is rigid in the spanwise direction. The thin plate deforms under fluid dynamic forces, making an angle θ with the freestream direction. The thrust force on the wing has been measured over a range of plate stiffnesses and oscillation frequencies. The variation of thrust coefficient with stiffness is shown in Fig. 1(b). Each of the three series corresponds to a different frequency. For each frequency, intermediate plate stiffness yields the greatest thrust force. Particle Image Velocimetry measurements revealed a correspondingly stronger jet vortex pattern. Chordwise flexibility is also found to bear efficiency benefits (Heathcote et al., 2004).

The progression to a study of spanwise flexibility follows naturally. Spanwise flexibility is of interest because the wings of birds and the fins of fish and aquatic mammals are flexible. One question is whether spanwise flexibility is beneficial to bird flight, or whether it is a limitation, due to the finite stiffness of the bone structure of the wing. Liu and Bose (1997) studied the effect of spanwise flexibility on the flukes of an immature fin whale, using inviscid calculations. The phase of the flexing motion relative to the heave was found to be a key parameter in determining the thrust and efficiency characteristics of the fin. In-phase motions yielded a benefit in efficiency and a significant increase in thrust. Out of phase motions were found to be detrimental. The subject of flexibility is particularly relevant to the design of miniature flapping wing aircraft, for which weight is a key restraint: light wings are inherently flexible.

The purpose of the present experimental study is to measure the effect of spanwise flexibility on the thrust and efficiency characteristics of a rectangular wing oscillated in heave. The heave amplitude, h, where $h = a_{\mathrm{ROOT}}/c = 0.175$, is constant for all experiments. Three additional dimensionless parameters may be defined: the Reynolds number, Garrick frequency, and Strouhal number based on the amplitude of the mid-span ($z = b/2$):

$$\mathrm{Re} = \frac{\rho U_0 c}{\mu}, \quad k_G = \frac{\pi fc}{U_0}, \quad \mathrm{Sr} = \frac{2fa_{\mathrm{MID}}}{U_0}.$$

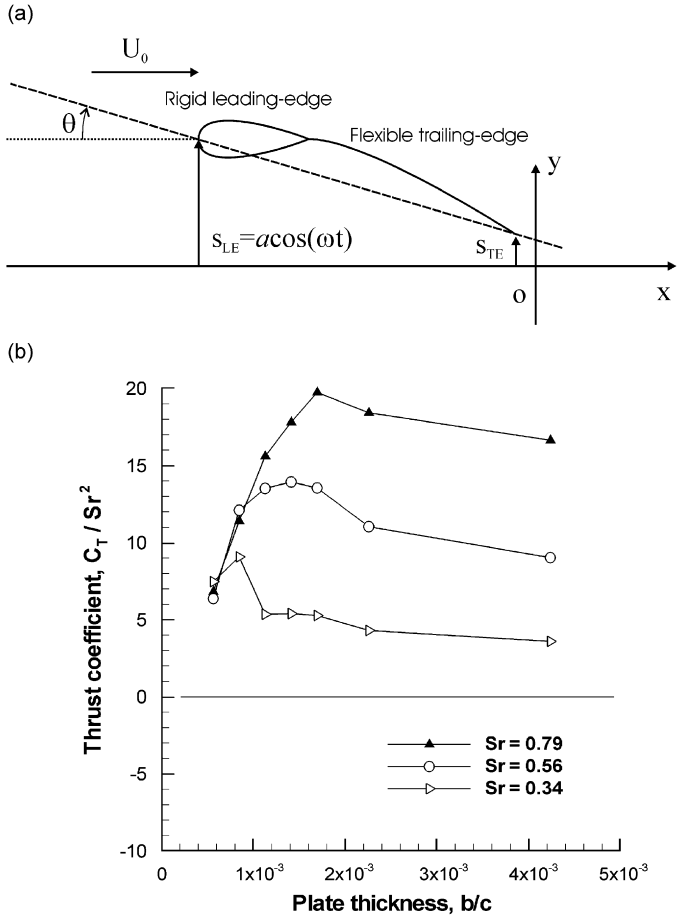

Fig. 1. (a) Schematic of the chordwise flexible airfoil heaving periodically; (b) thrust coefficient as a function of chordwise flexibility, Re = 9000. (Heathcote and Gursul, 2006).

2. Apparatus

2.1. Water tunnel

Experiments were conducted in a free-surface closed-loop water tunnel (Eidetics Model 1520) with a 381 mm wide × 508 mm deep test-section and flow speed range of 0–0.45 m/s. The free stream velocity was measured with a Laser Doppler Velocimetry system.

2.2. Driving mechanism

The driving mechanism is shown in Fig. 2(a). The wing was mounted vertically with one end attached to a horizontal shaker (Motovario 0.37 kW three-phase motor, 5:1 worm gear and IMO Jaguar controller). The displacement of the root is given by $s = a_{\mathrm{ROOT}}\cos(\omega t)$. A half-model wing with a splitter plate was tested. The wing is attached to a rod which moves in a narrow slit in the splitter plate. The splitter plate is submersed 0.08 m below the water's free surface. The splitter plate spans the width of the tunnel, and is 1.5 m long (of which 0.3 m extends upstream of the wing). The clearance between the wing root and the splitter plate is 2 mm. The gap between the wing tip and the glass floor of the water tunnel was $5c/3$, which corresponds to 56% of the semi-span.

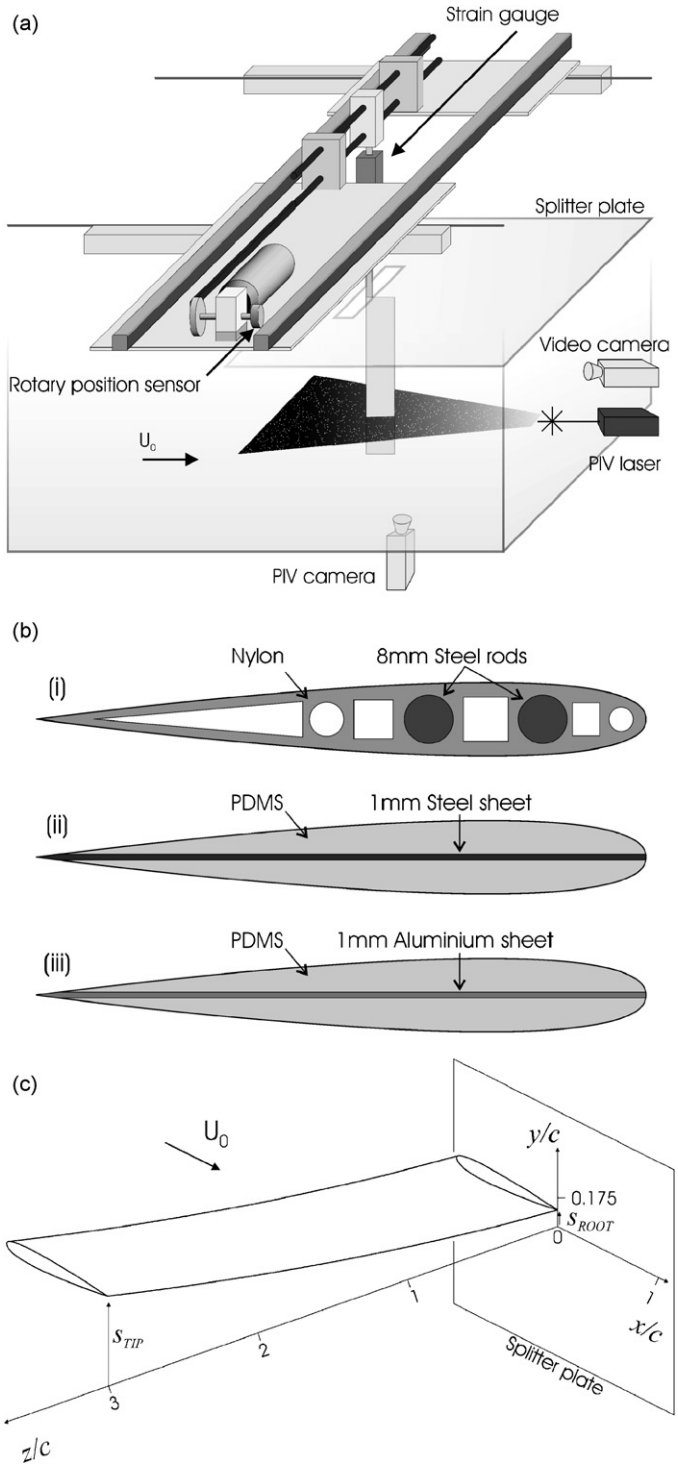

Fig. 2. (a) Water tunnel experimental set-up for force measurements, wing deformation measurements, and PIV measurements; (b) cross-sections of the three NACA0012 wings: (i) inflexible, (ii) flexible, (iii) highly flexible; (c) schematic of the spanwise flexible wing heaving periodically.

2.3. Wing construction

Three wings of 300 mm span, 100 mm chord, NACA0012 cross-section, and rectangular planform were constructed for the experiment. The first, termed *inflexible*, was designed to be as stiff as possible. The second, termed *flexible*, was designed to be of intermediate flexibility. The third, termed *highly flexible*, was designed to be overly flexible. Cross-sections of the three wings are shown in Fig. 2(b). The inflexible wing was constructed from nylon ($E = 5$ GPa) in a rapid prototyping machine. A hollowed structure and two 8 mm diameter steel rods ($E = 200$ GPa) spanning from root to tip ensure a high spanwise stiffness. The surface of the wing was sanded smooth. Each of the two flexible wings was constructed from polydimethylsiloxane rubber (PDMS, $E = 250$ kPa) cast in a NACA0012 mould. The flexible wing was stiffened with 1 mm stainless steel sheet ($E = 210$ GPa); the highly flexible wing was stiffened with 1 mm aluminium sheet ($E = 70$ GPa). The orientations of the wing and splitter plate are shown in Fig. 2(c). The arrangement may be considered to represent the semi-span of a 600 mm span wing. A second inflexible wing, of 400 mm span, was constructed in a rapid prototyping machine for a set of force measurement validation tests. All four wings were designed to be stiff in the chordwise direction. The degree of chordwise flexing in the experiment was observed to be negligible for all wings and all frequencies.

2.4. Force measurements

A binocular strain gauge force balance (Frampton et al., 2001), machined from aluminium, was used to make direct force measurements in the x and y directions. The position of the strain gauge is shown in Fig. 2(a).

2.5. Wing deformation measurements

The shape of the wing was recorded with a 50 frames per second, high shutter speed, digital video camera. The position of the camera is shown in Fig. 2(a).

2.6. PIV measurements

Particle Image Velocimetry measurements were carried out with a TSI PIV system. The system comprised a dual Nd:Yag 120 mJ laser, 8 bit greyscale 2048×2048 pixel digital camera, Insight v6 image processing software, and dual processor Xeon computer. Seeding was provided with 4 μm hollow glass particles. The positions of the PIV camera and laser are shown in Fig. 2(a). Image pairs were analysed with a fast Fourier transform algorithm (32×32 pixel window size, 50% overlap, 127×127 velocity vectors with a spatial resolution of $0.016c$).

3. Experimental methods

3.1. Force measurement

The forces applied to the wing in the x and y directions, F_x and F_y, were measured with two binocular strain gauges. The force F_x is equal to the drag (or thrust) on the wing. The force F_y is equal to the lift on the wing, plus a contribution arising from the inertia of the wing. This contribution is proportional to the wing acceleration, and therefore does not contribute to the time-averaged power-input. The period-averaged power input therefore equals the period-averaged value of $F_y v$, where v is the instantaneous velocity of the root. This approach was validated as will be discussed later in the paper.

Drive force and thrust force data were collected for 60 oscillations (sample rate 1 kHz) for each test condition. The thrust coefficient, C_T, is given by

$$C_T = \frac{T}{\frac{1}{2}\rho U_0^2 c},$$

where T is the thrust per unit span. The time-averaged thrust coefficient is found by averaging over a complete number of cycles. The time-averaged power input is given by

$$\overline{C}_P = \frac{\overline{F_y v}}{\frac{1}{2}\rho U_0^3 c},$$

where $F_y v$ is the instantaneous power input, and the overbar denotes an average over time. The propulsive efficiency is given by

$$\eta = \frac{\overline{T}U_0}{\overline{F_y v}} = \frac{\overline{C}_T}{\overline{C}_P}.$$

3.2. Force measurement uncertainty

Since the fluid dynamic forces acting on the wing may vary along the span, it is important that the strain gauge is sensitive only to force, and insensitive to the distance from the gauge at which the force acts. Insensitivity to bending moment is a key feature of a binocular strain gauge. It was found during the calibration tests that the uncertainty in F_x and F_y induced by a typical range of bending moments was less than 0.5%. Coupling effects—fictitious indicated forces in the x direction due to loading in the y direction, and *vice versa*—were found to give rise to a 2% uncertainty. The uncertainty due to torque about the z-axis was found to be 1%. The uncertainty from temperature variations was found to be negligible. The response of the gauge was found to be linear (1% uncertainty) over the experimental range. The combined uncertainty in the strain gauge readings is approximately 3%. Since the efficiency readings depend on readings of both F_x and F_y, the uncertainty in the efficiency data is approximately 6%.

3.3. Wing deformation

Since in all experiments the bending mode was observed to be first order, the deformation of the wing is described by the tip amplitude and tip phase, relative to the amplitude and phase of the root. Specialist motion-tracking software (RealViz MatchMover Pro 3.1) returned the coordinates of the root and tip in each frame. After the initial transients, the positions of the root and tip were recorded over eight oscillations. The phase and amplitude of the root and tip were found with a cosine fit.

3.4. PIV measurements

Velocity fields were captured for all three wings (inflexible, flexible, highly flexible), six spanwise locations ($z/c = 0.5$, 1, 1.5, 2, 2.5, and 2.85), and two points in the motion ($s_{\mathrm{ROOT}} = +a$ and $s_{\mathrm{ROOT}} = 0$), yielding a total of 36 cases. For each case, 50 image pairs were captured, each at the same point in the cycle. An ensemble average was formed, from which the vorticity field for that case was calculated.

4. Force measurement validation

In order to validate the force measurement system, a set of thrust and power-input measurements were carried out for a 100 mm chord, 400 mm span, NACA0012 airfoil, oscillating with constant amplitude ($h = 0.175$) between two end plates. Tests were carried out for Reynolds numbers of 10 000, 20 000, and 30 000, and for a frequency range of $0 < k_G < 7$. The thrust coefficient, power-input coefficient, and propulsive efficiency data are plotted in Fig. 3, in parts (a), (b), and (c), respectively. Also shown for comparison are the predictions of Garrick (1936), a panel method, and a viscous Navier–Stokes code (run for $\mathrm{Re} = 20\,000$, $M = 0.05$, laminar flow). The panel method and Navier Stokes predictions are of Young (2005), and Young and Lai (2004), and the reader is referred to these sources for details of the method. To match the parametric range of the present experimental data, additional calculations were performed by Young (2006).

It is seen from Fig. 3(a) that the Navier–Stokes predictions for thrust coefficient are in very close agreement with the experimental values over the complete frequency range. A degree of confidence is therefore conferred in the thrust–force measurement apparatus. Furthermore, close agreement is found between the measured drag coefficient ($C_D = 0.028$) and the values found in previous experiments by Sheldahl and Klimas (1981) ($C_D = 0.0245$) and Koochesfahani (1989) ($C_D = 0.027$). A number of additional observations may be made in Fig. 3(a). Firstly, the experimental data shows the effect of Reynolds number to be very small for the range $10\,000 < \mathrm{Re} < 30\,000$. Secondly, the panel method predicts marginally higher thrust coefficients than Garrick theory, consistent with the findings of Jones et al. (2001b). Both inviscid methods overestimate the experimentally measured thrust coefficient.

It is seen in Fig. 3(b) that close agreement is observed between the experimental and Navier–Stokes predictions for power-input coefficient. Here again, the effect of Reynolds number is observed to be small for the experimental data.

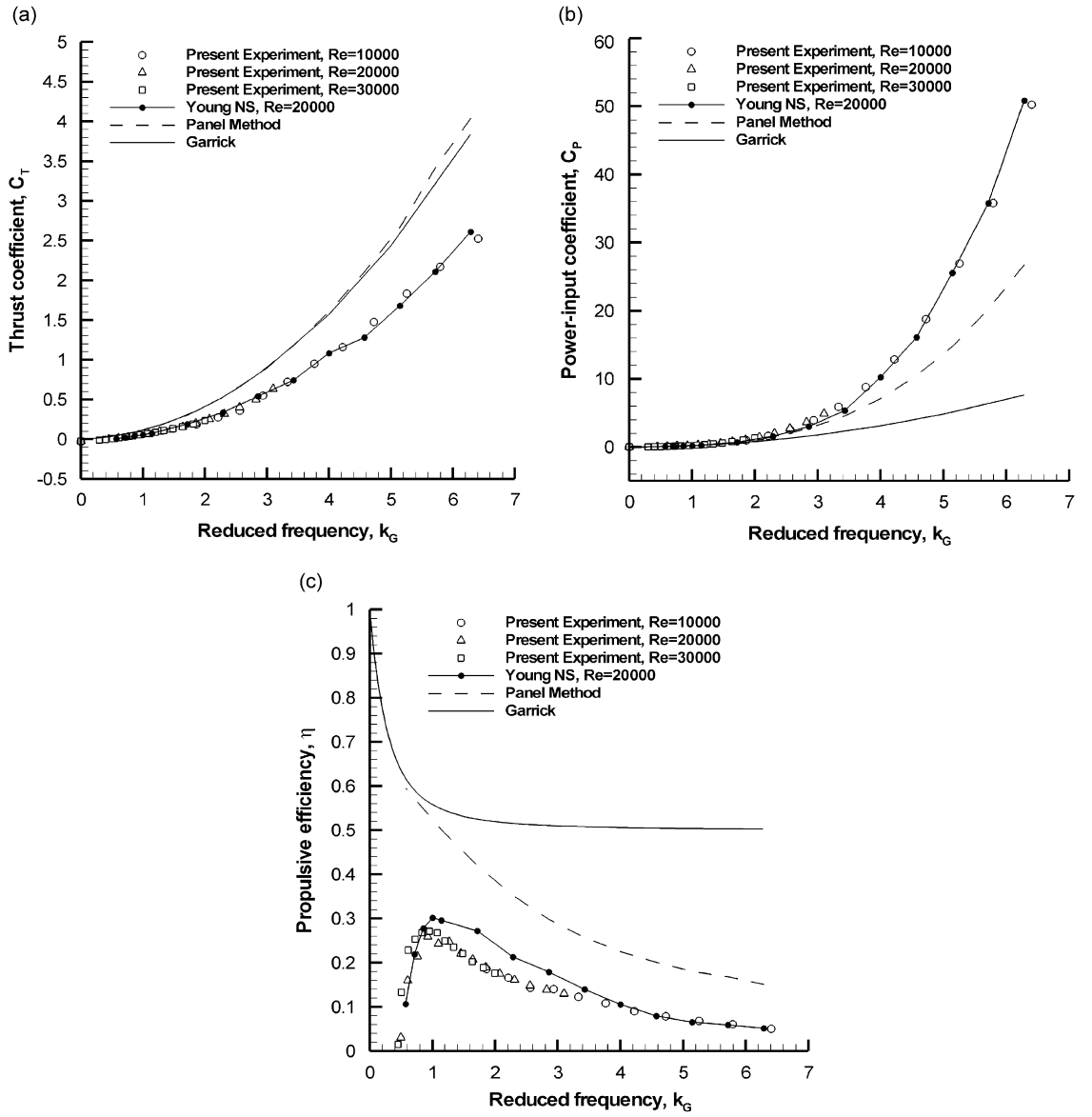

Fig. 3. Comparison of present force validation experimental data (2-D NACA0012 airfoil in pure heave) with linear theory, panel method and Navier Stokes solver. (a) Thrust coefficient; (b) power-input coefficient; (c) propulsive efficiency.

Garrick theory and the panel method are seen to underestimate the power-input coefficient, particularly severely in the case of Garrick theory. Young and Lai (2004) showed the key limitation of the panel method to be the absence of a model of leading-edge vorticity shedding; leading-edge vortices in the Navier–Stokes model were shown to augment the surface pressures, leading to a greater power-input requirement. This limitation is shared by Garrick theory, which is further afflicted, as described by Jones et al. (2001b), by an overly simplistic model of the shedding of trailing-edge vorticity.

Propulsive efficiency—the ratio of thrust coefficient to power-input coefficient—is shown in Fig. 3(c). Although the panel method correctly predicts a decrease in efficiency with increasing frequency (Garrick theory predicts the efficiency to tend to a value of 0.5), both inviscid methods are seen to significantly overestimate efficiency. It is seen from Fig. 3 (a) and (b) that the inaccuracy of the inviscid methods results primarily from the power-input coefficient predictions. Reasonable agreement is observed between the experiments and Navier–Stokes simulations. In particular, close

agreement is found in the trend towards drag (negative efficiency) at low frequencies, the peak efficiency ($\eta \approx 30\%$), and the optimum frequency ($k_G \approx 1$).

5. Results and discussion

The results of a parametric study of the effect of spanwise flexibility, Reynolds number and frequency are discussed in this section. Special attention is given to the effect of flexibility in the single case of $\mathrm{Re} = 30\,000$, $k_G = 1.82$.

5.1. Deformation—single case

The shape response of the three wings for the single case of $\mathrm{Re} = 30\,000$, $k_G = 1.82$ is represented in Fig. 4. The tip displacements of the three wings are plotted over a period of two cycles. Symbols represent experimental data points. Cosine wave curve fits for the three wing tips, and for the root are drawn. The cosine fit is seen to be a good approximation to the displacement of the tip, indicating the suitability of representing the tip displacement in the form $a_{\mathrm{TIP}}\cos(\omega t + \phi)$. The wing tip curves lie to the right of the root displacement curve, indicating a negative value of the tip phase angle φ. The plot illustrates the steep increase in tip amplitude moving from the inflexible to the flexible wing, with only a small increase in tip phase lag, and the slight increase in tip amplitude moving from the flexible to the highly flexible wing, with a large increase in tip phase lag. The tip amplitudes and phase angles for the three flexibilities are summarized in Table 1.

5.2. Deformation—parametric study

The variation of the shape response with Reynolds number and frequency is presented in Fig. 5. In Fig. 5(a) the variation of tip amplitude with frequency is shown for a single Reynolds number. The displacement of the wing tip may be considered to arise from the sum of the root displacement and the deformation of the wing. The amplitude of the wing tip therefore depends on the amplitude of the root, and the amplitude and phase of the deformation. The variation of tip phase with frequency is plotted in Fig. 5(b) for the same Reynolds number. In Fig. 5(c) the frequency parameter is eliminated: tip amplitude is plotted against tip phase. In addition, the data for all three Reynolds numbers were included. Each data point corresponds to a test at a different frequency; the direction of increasing frequency is indicated. It is noted that the case of Fig. 4 ($\mathrm{Re} = 30\,000$, $k_G = 1.82$) corresponds to the right-most data point on the k_G axes of Fig. 5(a) and (b), and of the right-most data point on the phase axis of Fig. 5(c). It is seen in Fig. 5(a) that the normalized tip amplitude of all three wings tends to unity as the frequency approaches zero. It is also seen that the tip

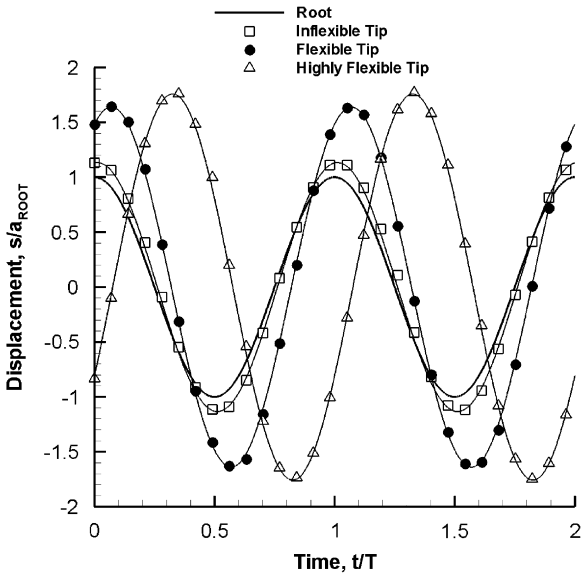

Fig. 4. Tip displacements as a function of time, $\mathrm{Re} = 30\,000$, $k_G = 1.82$.

Table 1
Displacement and force data for the three wings; Re = 30 000

Wing	k_G	Sr	a_{TIP}/a_{ROOT}	ϕ	C_T	C_P	η
Inflexible	1.82	0.234	1.13	−4.2°	0.21	1.23	0.17
Flexible	1.82	0.280	1.64	−25.1°	0.32	1.88	0.17
Highly flexible	1.82	0.162	1.76	−117°	0.11	0.79	0.14

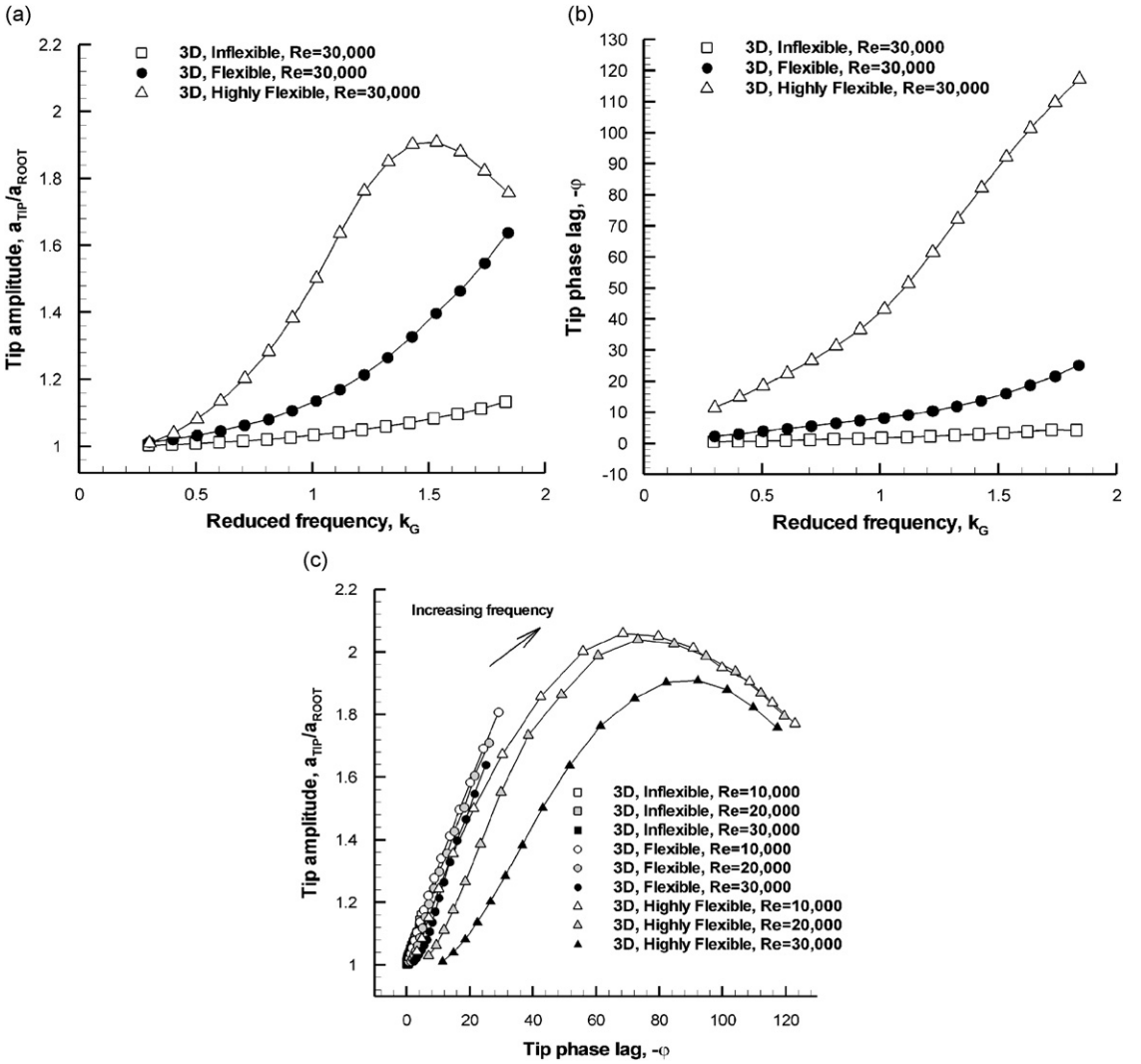

Fig. 5. (a) Tip amplitude as a function of Garrick frequency, Re = 30 000; (b) tip phase lag as a function of Garrick frequency, Re = 30 000; (c) tip amplitude as a function of tip phase lag.

amplitude of both the inflexible and flexible wings increases with oscillation frequency over the whole frequency range. The rate of increase is initially small, but increases with frequency. The tip amplitude of the highly flexible wing increases moderately quickly for low frequencies, and rapidly at intermediate frequencies. At higher frequencies the tip amplitude reaches a maximum and then decays. The reason for the peak in tip amplitude may be seen with reference to Fig. 5(b), in which tip phase angle is plotted against frequency. The highly flexible wing is observed to behave strikingly

differently to the inflexible and flexible wings: the phase delay of the wing tip is far higher throughout the whole frequency range. With increasing frequency, the deformation of the wing increases (favourable in terms of the tip amplitude) but the point in the cycle at which the greatest deformation occurs becomes rapidly unfavourable. Fig. 5(a) and (b) indicate that the amplitude becomes maximum with a phase angle of 90° around $k_G \approx 1.5$ for the highly flexible wing. Hence the resonant structural frequency of the highly flexible wing in the first mode is around $k_G \approx 1.5$. On the other hand, for the flexible wing, the test frequency appears to be always less than the resonant frequency in the range tested. The difference between the highly flexible wing and the inflexible and flexible wings is further illustrated with reference to Fig. 5(c). The inflexible and flexible wing data lie on a line (the inflexible data points are obscured by the flexible ones), whereas the highly flexible data points lie on three curves, which generally lie to the right of the line (there is a small degree of overlap).

5.3. Thrust force—single case

Instantaneous thrust coefficient curves for the case $\mathrm{Re} = 30\,000$, $k_G = 1.82$, are shown in Fig. 6. Two peaks in thrust are consistent with symmetry of the geometry, and the shedding of two vortices per cycle (Heathcote and Gursul, 2004). It is seen that the thrust coefficient of the flexible wing is greater than that of the inflexible wing, indicating that introducing a degree of spanwise flexibility increases the thrust coefficient for this Reynolds number and frequency. It is also seen that the thrust coefficient of the highly flexible wing is the lowest of the three. Two interesting features are observed for the highly flexible wing. Firstly, small amplitude oscillations in thrust are observed and, secondly, the instantaneous thrust coefficient is always positive. The large deformation of the wing, and the different velocities (and hence effective angles of attack) along the span, may create an interesting vortex shedding pattern. The time-averaged thrust coefficients are shown in Table 1. Compared to the inflexible wing, the flexible wing experiences a 50% thrust benefit, whereas the highly flexible wing experiences a 50% deficit.

In summary, the flexibility of a wing is seen to greatly affect the thrust characteristics of the wing. The tip phase angle is seen to be an important parameter: despite the tip amplitude being approximately equal for the flexible and highly flexible wings, the forces differ by a factor of three.

5.4. PIV study

A scale diagram of the three wings at the point when the root is stationary at $s = +a$ ($t/T = 0$) is shown in Fig. 7(a). The tip of the inflexible wing is stationary at this point, and the tips of the flexible and highly flexible wings are moving upwards. Arrows are drawn to indicate the direction of motion of the wing tip. The phase of the highly flexible wing is such that the y-displacement of the tip is still negative. Vorticity fields at six planes along the span are shown in Fig. 7(b) for each of the three wings. The direction of the free stream velocity is along the positive x axis, as shown in Fig. 7(a). To minimise the degree of overlap of the vorticity fields, the z axis is scaled differently to the x and y axes. For each of

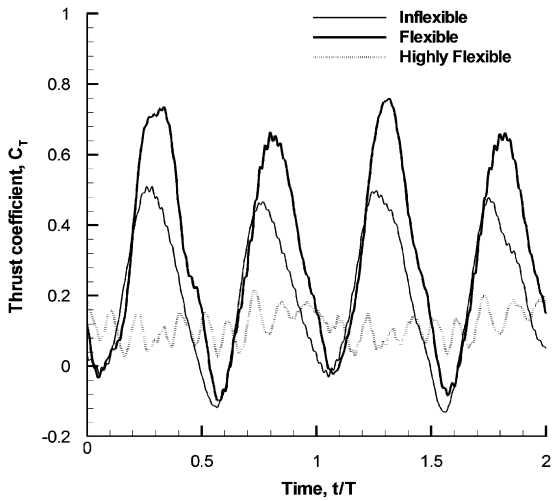

Fig. 6. Instantaneous thrust coefficient as a function of time over two heave cycles; $\mathrm{Re} = 30\,000$, $k_G = 1.82$.

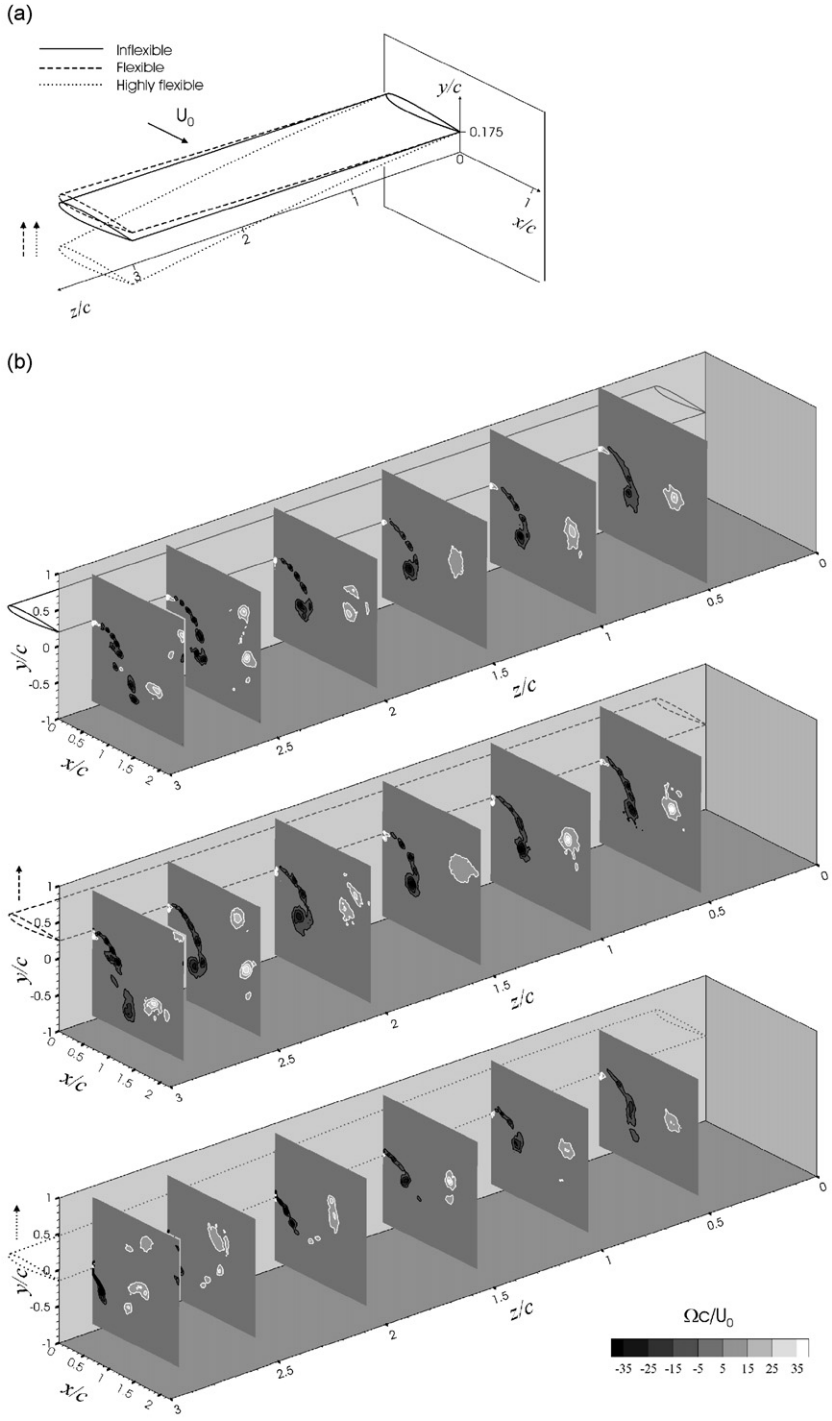

Fig. 7. (a) Scale drawing of the inflexible, flexible, and highly flexible wings; (b) corresponding vorticity fields downstream of the trailing edge; $\mathrm{Re} = 30\,000$, $k_G = 1.82$, $t/T = 0$. Dimensionless vorticity contours plotted are -35, -25, -15, -5, 5, 15, 25, 35.

the three wings, the trailing-edge of the root is located at $x/c = 0$, $y/c = 0.175$, $z/c = 0$. The y coordinate of each wing then varies along the span according to the wing stiffness. Clockwise (looking in the direction of increasing z) vorticity is shown light; anti-clockwise vorticity is shown dark. For clarity, regions of positive and negative vorticity are separated by white and black lines, respectively.

Near the root of the inflexible wing ($z/c = 0.5$), two vortices of opposite sign are visible. Previous studies of two-dimensional oscillating airfoils have found very similar vortical flow patterns. Studies in the literature over a greater streamwise distance have shown that the pattern of alternating vortices continues. How far in the streamwise and

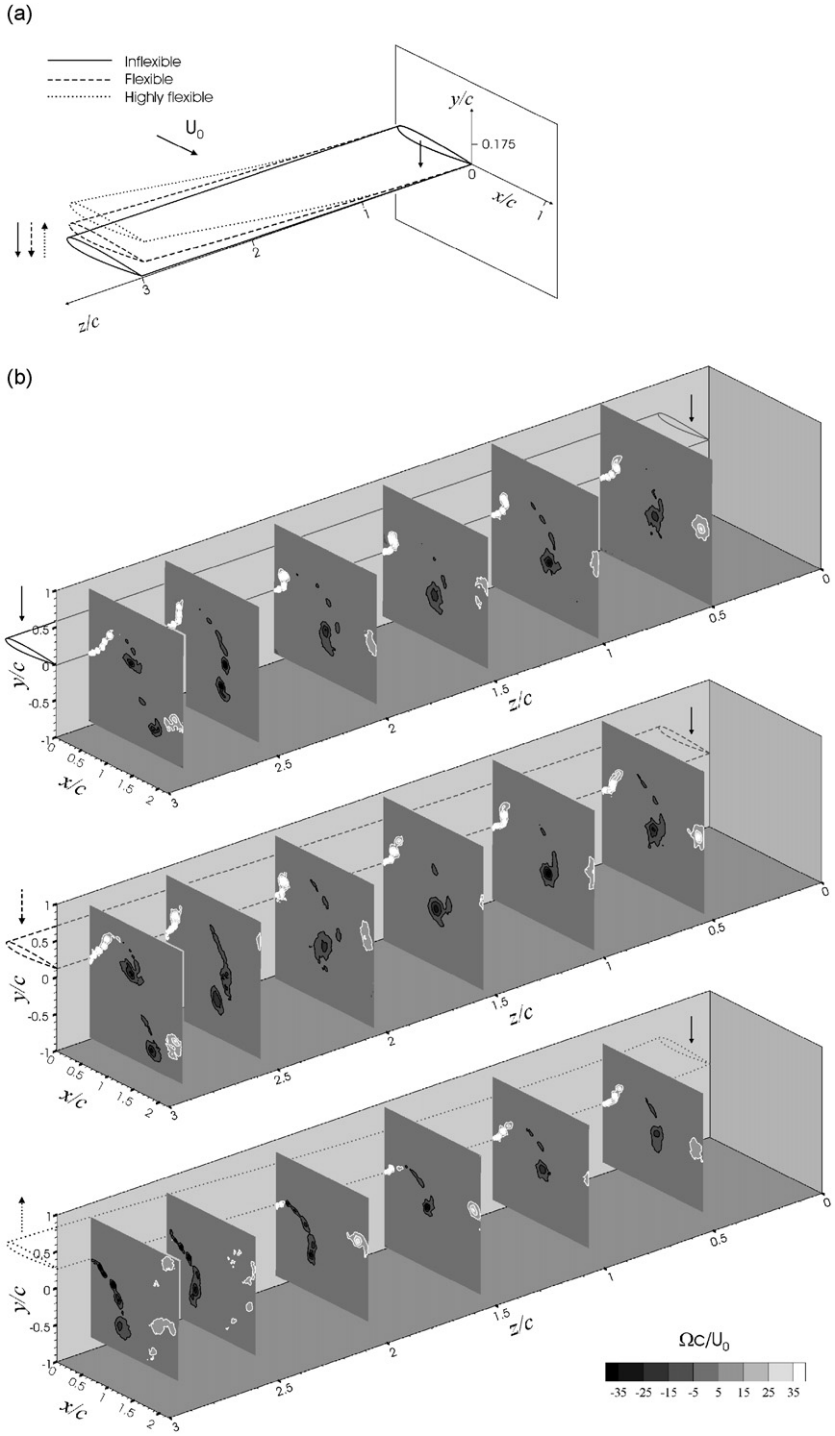

Fig. 8. (a) Scale drawing of the inflexible, flexible, and highly flexible wings; (b) corresponding vorticity fields downstream of the trailing edge; $\mathrm{Re} = 30\,000$, $k_G = 1.82$, $t/T = 1/4$. Dimensionless vorticity contours plotted are -35, -25, -15, -5, 5, 15, 25, 35.

spanwise directions the *reverse von Kármán street* persists in the present case is likely to depend on the aspect ratio of the wing. The vorticity pattern at $z/c = 1$ is similar to the pattern at $z/c = 0.5$. Nearer the tip, however, a more complex pattern emerges: The clockwise (light shading) vortex forks into two branches. One branch lies above the $y/c = 0$ plane, and one branch lies below. Chains of inclined and interconnected vortex loops over oscillating wings of finite aspect ratio have been reported previously (Brodsky, 1994; Emblemsvag et al., 2003; Bozkurttas et al., 2006; Platzer and Jones, 2006). The forking pattern observed in a spanwise plane near the tip is due to this pattern of vortex loops.

Returning to the vorticity field near the root ($z/c = 0.5$), it is seen that the pattern of the flow is similar for each of the three wings, although the magnitude of the vorticity appears strongest in the case of the flexible wing, and weakest in the case of the highly flexible wing. This trend also holds for $z/c = 1$. As for the inflexible wing, the clockwise vortex forks into two distinct vortices for the flexible case. The pattern is qualitatively different in the case of the highly flexible wing, however, where the vortex fragments into a collection of weak vortices. The reason for this behaviour may be investigated with reference to Fig. 8, which shows the vorticity patterns one quarter of a cycle later ($t/T = 1/4$), when the root is moving downwards through the origin. Fig. 8(a) illustrates that while the tips of the inflexible and flexible wings move in the same direction as the root at this point in time, the tip of the highly flexible wing moves in the

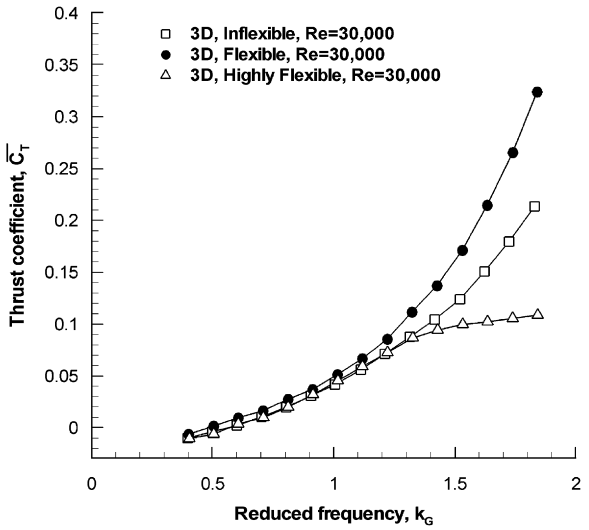

Fig. 9. Thrust coefficient as a function of Garrick frequency, Re = 30 000.

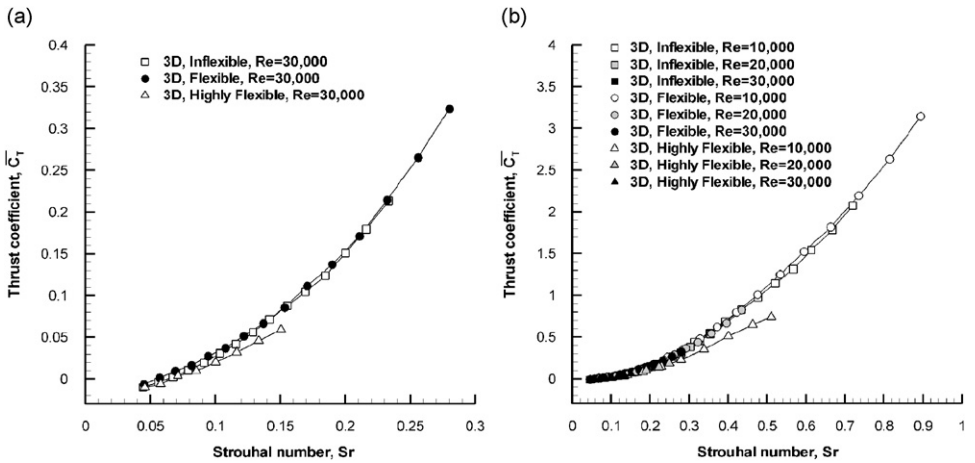

Fig. 10. Thrust coefficient as a function of Strouhal number based on the excursion of the mid-span, $|\phi| < 60°$: (a) Re = 30 000, (b) all Reynolds numbers.

opposite direction. The effect on the flow field is shown in Fig. 8(b), where for the highly flexible wing it is seen that the sense of vorticity shed at the root is opposite to that shed near the tip. The resulting complex vorticity pattern is likely to be responsible for the multiple peaks observed in the thrust coefficient time history (Fig. 6). As in the case of Fig. 7, the magnitude of the vortex near the root appears to be greatest in the case of the flexible wing, and least in the case of the highly flexible wing.

5.5. Force—parametric study

In order to establish whether the flexible wing experiences greater thrust over a range of Reynolds numbers and frequencies, a parametric study was carried out. The complete set of thrust coefficient data for $\mathrm{Re} = 30\,000$ is plotted in Fig. 9. The single case discussed above corresponds to the highest frequency in Fig. 9. It is seen that the benefit in thrust for the flexible wing over the inflexible wing persists to lower frequencies, and likewise for the decrement in thrust for the highly flexible wing. At the lowest frequencies the wings experience drag.

An alternative to the Garrick frequency parameter k_G is the Strouhal number, Sr. With the concept of effective amplitude, the characteristic length chosen here is the amplitude of the mid-span, giving $\mathrm{Sr} = 2fa_{\mathrm{MID}}/U_0$. It is noted

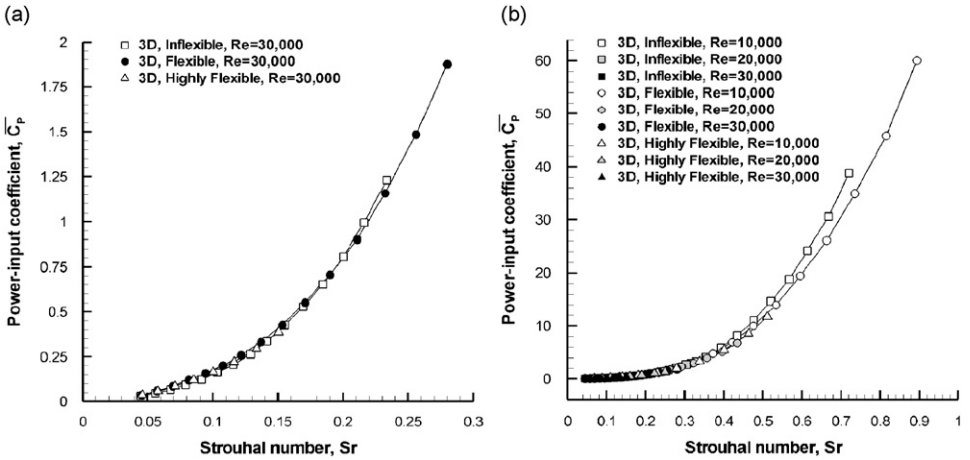

Fig. 11. Power-input coefficient as a function of Strouhal number based on the excursion of the mid span, $|\phi| < 60°$: (a) $\mathrm{Re} = 30\,000$, (b) all Reynolds numbers.

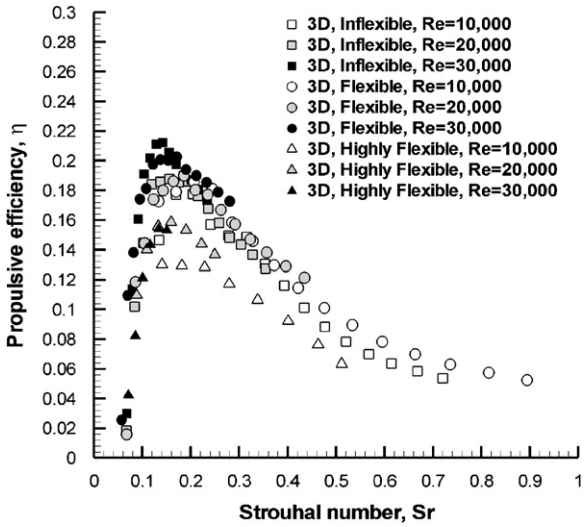

Fig. 12. Propulsive efficiency as a function of Strouhal number, $|\phi| < 60°$.

that the quantity is closely related to the peak effective angle of attack at the mid-span, $\tan^{-1}(2\pi f a_{\mathrm{MID}}/U_0)$. From here on, the Strouhal number will supersede the Garrick frequency. For high tip phase lags the physical meaning of the Strouhal number expires (for out of phase motions the amplitude of the mid point may be very small, but the amplitude of the root and tip may be large). For this reason, data for which the tip phase angle exceeds 60° is omitted. The data points omitted may be seen with reference to Fig. 5(c) (for $|\phi| > 60°$).

In Fig. 10(a), the thrust coefficient is plotted against Strouhal number. A striking feature is that the thrust coefficient curves for the inflexible and flexible wings show near collapse. This indicates the appropriateness of the Strouhal number for characterising the thrust coefficient of stiff to moderately flexible wings. Plots for all Reynolds numbers are shown in Fig. 10(b). Near collapse of the data is seen for the inflexible and flexible wings. The flexible wing is observed to experience a marginally higher thrust coefficient for high Strouhal numbers. Only a very weak Reynolds number dependence is observed. The highly flexible wing is seen to deviate from the inflexible and flexible data. The divergence is greatest for the highest tip phase lags.

In summary, the thrust coefficient is found to be a function of Strouhal number based on the amplitude of the mid-span of the wing, and to be a very weak function of Reynolds number.

5.6. *Power input*

Power-input coefficient is plotted as a function of Strouhal number for Re = 30 000 in Fig. 11(a). Near complete data collapse is observed for all wings, showing that the Strouhal number is appropriate for characterising the power requirements of the heave motion, as well as the thrust characteristics. A marginally higher power coefficient for the inflexible wing at high Strouhal numbers is observed. In Fig. 11(b) the power input coefficient is plotted for all Reynolds numbers. Power coefficient is seen to be independent of Reynolds number. Again, a marginally higher power coefficient for the Inflexible wing at high Strouhal numbers is noted.

5.7. *Efficiency*

Propulsive efficiency is plotted as a function of Strouhal number in Fig. 12. The peak in efficiency occurs at a Strouhal number of between 0.14 and 0.18, and has a value of approximately 21%, lower than the 27% found for the 2-D case (see Fig. 3(c)). The efficiency increases slightly with Reynolds number, consistent with diminishing viscous effects. Around the peak in efficiency the inflexible and flexible wings perform similarly and the highly flexible wing performs poorly. At higher Strouhal numbers, the flexible wing has the highest propulsive efficiency. The origin is a slightly higher thrust, and moderately lower power requirement. It is noted that the range of Strouhal numbers over which a degree of flexibility is beneficial overlaps the Strouhal number range of birds, bats, insects, fish and aquatic

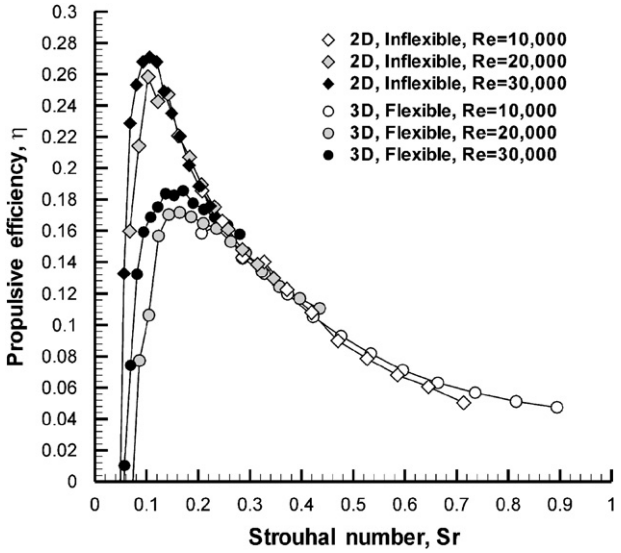

Fig. 13. Comparison of propulsive efficiency as a function of Strouhal number for 2-D inflexible and 3-D flexible cases.

mammals ($0.2 < Sr < 0.4$) (Taylor et al., 2003). This suggests that wing flexibility may be beneficial to bird flight aerodynamically, and is also of relevance to the design of micro air vehicles.

A further interesting comparison is between the efficiency of the inflexible two-dimensional case and the flexible three-dimensional case. The two sets of curves are shown in Fig. 13. The Strouhal number at which the peak in efficiency occurs is slightly lower for the two-dimensional case. For Strouhal numbers greater than approximately 0.25, the 2-D inflexible and 3-D flexible cases yield similar efficiencies.

6. Conclusions

A study of the effect of spanwise flexibility on the thrust, power-input, and propulsive efficiency of a rectangular wing has been performed. The wing has an aspect ratio of 6, and was oscillated in heave at one end. Experiments were carried out in a water tunnel over a Reynolds number range of 10 000–30 000. A two-component force balance was used to obtain the thrust and efficiency characteristics of the wing. Three wings of varying spanwise stiffness were tested. All were rigid in the chordwise direction.

When the thrust coefficient was plotted against reduced frequency, a limited degree of flexibility was observed to be greatly beneficial. A thrust benefit of 50% was observed for a wing of intermediate flexibility. For a highly flexible wing, however, the tip was observed to move out of phase with the root, and a diminished thrust coefficient was recorded.

PIV measurements at a number of spanwise locations showed a reverse von Kármán vortex street near the wing root, resembling the flow pattern observed in 2-D studies in the literature. Near the tip, the vortices were observed to fork into two branches. Such vortex branching due to interconnected loops has been observed previously. The initial rise in thrust coefficient with the introduction of spanwise flexibility was seen from the vorticity fields to arise from an increase in the effective heave amplitude. Excessive spanwise flexibility was seen to lead to large tip phase lags, where the root and tip moved in opposite directions for significant portions of the stroke. The corresponding vorticity fields revealed the formation of vorticity of one sense near the root, and of opposite sense near the tip, leading to a fragmented and weak vorticity pattern. Significantly lower thrust coefficients, and diminished efficiencies, were observed in this regime.

When a Strouhal number was defined based on the amplitude of the mid-span, benefits to flexibility were observed for Strouhal numbers greater than approximately 0.2. The wing of intermediate flexibility was observed to experience a marginally higher thrust coefficient, and marginally lower power-input coefficient, leading to a gain in efficiency. It was noted that Strouhal numbers in nature range from 0.2 to 0.4. The overly flexible wing was characterised by large tip phase lags, and performed relatively poorly. A slight increase in efficiency with Reynolds number was observed, consistent with declining viscous effects.

The findings of this paper suggest that birds, bats and insects may benefit aerodynamically from the flexibility of their wings. From a design aspect, flexibility may benefit Micro Air Vehicles both aerodynamically and in the inherent lightness of flexible structures.

Acknowledgements

This work has been supported by an EPSRC (Engineering and Physical Sciences Research Council) studentship, as well as a RCUK Academic Fellowship in Unmanned Air Vehicles. The authors are grateful to Alastair Burls for the design and construction of the flexible wings.

References

Anderson, J.M., Streitlien, K., Barrett, D.S., Triantafyllou, M.S., 1998. Oscillating foils of high propulsive efficiency. Journal of Fluid Mechanics 360, 41–72.

Betz, A., 1912. Ein Beitrag zur Erklaerung des Segelfluges. Zeitschrift fuer Flugtechnik und Motorluftschiffahrt 3, 269–272.

Bozkurttas, M., Dong, H., Mittal, R., Madden, P., Lauder, G. V., 2006. Hydrodynamic performance of deformable fish fins and flapping foils. AIAA Paper 2006-1392, 44th AIAA Aerospace Sciences Meeting and Exhibit.

Brodsky, A.K., 1994. The evolution of insect flight. Oxford University Press, New York.

Emblemsvag, J. E., Suzuki, R., Candler, G. V., 2003. Simulation of a three-dimensional flapping cantilever for micro air vehicle propulsion. AIAA Paper 2003–4012, 33rd AIAA Fluid Dynamics Conference.

Frampton, K.D., Goldfarb, M., Monopoli, D., Cveticanin, D., 2001. Passive aeroelastic tailoring for optimal flapping wings. In: Mueller, T.J. (Ed.), Fixed and Flapping Wing Aerodynamics for Micro Air Vehicle Applications. Progress in Astronautics and Aeronautics, vol. 185. AIAA, Virginia, pp. 473–482.

Freymuth, P., 1990. Thrust generation by an airfoil in hover modes. Experiments in Fluids 9, 17–24.
Garrick, I. E., 1936. Propulsion of a flapping and oscillating airfoil. NACA 567.
Heathcote, S., Gursul, I., 2004. Jet switching phenomenon for a plunging airfoil. AIAA Paper 2004-2150, 34th AIAA Fluid Dynamics Conference and Exhibit.
Heathcote, S., Gursul, I., 2006. Flexible flapping airfoil propulsion at low Reynolds numbers. Accepted for publication in the AIAA Journal. Also, see AIAA Paper 2005-1405, 43rd AIAA Aerospace Sciences Conference and Exhibit, 2005.
Heathcote, S., Martin, D., Gursul, I., 2004. Flexible flapping airfoil propulsion at zero freestream velocity. AIAA Journal 42, 2196–2205.
Hover, F.S., Haugsdal, O., Triantafyllou, M.S., 2004. Effect of angle of attack profiles in flapping foil propulsion. Journal of Fluids and Structures 19, 37–47.
Isogai, K., Shinmoto, Y., Watanabe, H., 1999. Effects of dynamic stall on propulsive efficiency and thrust of flapping airfoil. AIAA Journal 37, 1145–1151.
Jones, K.D., Dohring, C.M., Platzer, M.F., 1998. Experimental and computational investigation of the Knoller-Betz effect. AIAA Journal 36, 1240–1246.
Jones, K. D., Duggan, S. J., Platzer, M. F., 2001a. Flapping-wing propulsion for a micro air vehicle. AIAA Paper 2001-0126, 39th Aerospace Sciences Meeting & Exhibit.
Jones, K.D., Lund, T.C., Platzer, M.F., 2001b. Experimental and computational investigation of flapping wing propulsion for micro air vehicles. Fixed and flapping wing aerodynamics for micro air vehicle applications. In: Mueller, T.J. (Ed.), Progress in Astronautics and Aeronautics, Vol. 195. AIAA, Virginia, pp. 307–339.
Jones, K. D., Castro, B. M., Mahmoud, O., Pollard, S. J., Platzer, M. F., Neef, M. F., Gonet, K., Hummel, D., 2002. A collaborative numerical and experimental investigation of flapping-wing propulsion. AIAA Paper 2002-0706, 40th Aerospace Sciences Meeting & Exhibit.
Katzmayr, R., 1922. Effect of periodic changes of angle of attack on behaviour of airfoils. NACA 147.
Knoller, R., 1909. Die Gesetze des Luftwiderstandes. Flug- und Motortechnik (Wien) 3, 1–7.
Koochesfahani, M.M., 1989. Vortical patterns in the wake of an oscillating airfoil. AIAA Journal 27, 1200–1205.
Lai, J.C.S., Platzer, M.F., 1999. Jet characteristics of a plunging airfoil. AIAA Journal 37, 1529–1537.
Lighthill, M.J., 1970. Aquatic animal propulsion of high hydromechanical efficiency. Journal of Fluid Mechanics 44, 265–301.
Liu, P., Bose, N., 1997. Propulsive performance from oscillating propulsors with spanwise flexibility. Proceedings of the Royal Society London 453, 1763–1770.
Maxworthy, T., 1981. The fluid dynamics of insect flight. Annual Review of Fluid Mechanics 13, 329–350.
Platzer, M. F., Jones, K. D., 2006. Flapping wing aerodynamics—progress and challenges. AIAA Paper 2006-500, 44th AIAA Aerospace Sciences Meeting and Exhibit.
Ramamurti, R., Sandberg, W.C., 2001. Simulation of flow about flapping airfoils using finite element incompressible flow solver. AIAA Journal 39, 253–260.
Sheldahl, R. E., Klimas, P. C., 1981. Aerodynamic characteristics of seven symmetrical airfoil sections through 180-degree angle of attack for use in aerodynamic analysis of vertical axis wind turbines. Sandia National Laboratories.
Shyy, W., Berg, M., Ljungqvist, D., 1999. Flapping and flexible wings for biological and micro air vehicles. Progress in Aerospace Sciences 35, 455–505.
Spedding, G.R., Lissaman, P.B.S., 1998. Technical aspects of microscale flight systems. Journal of Avian Biology 29, 458–468.
Sunada, S., Kawachi, K., Matsumoto, A., Sakaguchi, A., 2001. Unsteady forces on a two-dimensional wing in plunging and pitching motions. AIAA Journal 39, 1230–1239.
Taylor, G.K., Nudds, R.L., Thomas, A.L.R., 2003. Flying and swimming animals cruise at a Strouhal number tuned for high power efficiency. Nature 425, 707–711.
Triantafyllou, M.S., Triantafyllou, G.S., Yue, D.K.P., 2000. Hydrodynamics of fishlike swimming. Annual Review of Fluid Mechanics 32, 33–53.
Tuncer, I.H., Platzer, M.F., 1996. Thrust generation due to airfoil flapping. AIAA Journal 34, 324–331.
Wootton, R.J., 1981. Support and deformability in insect wings. Journal of Zoology London 193, 447–468.
Wu, T.Y., 1971. Hydromechanics of swimming propulsion, part 2: some optimum shape problems. Journal of Fluid Mechanics 46, 521–544.
Young, J., 2005. Numerical simulation of the unsteady aerodynamics of flapping airfoils. Ph.D. Dissertation, School of Aerospace, Civil and Mechanical Engineering, New South Wales University, Canberra.
Young, J., 2006. Private communication.
Young, J., Lai, J.C.S., 2004. Oscillation frequency and amplitude effects on the wake of a plunging airfoil. AIAA Journal 42, 2042–2052.